




Quantifying the mechanical effects of He, W and He + W ion irradiation on tungsten with spherical nanoindentation

Jordan S. Weaver¹ , Cheng Sun^{2,3}, Yongqiang Wang², Surya R. Kalidindi⁴, Russ P. Doerner⁵, Nathan A. Mara^{1,6,*}, and Siddhartha Pathak^{7,*}

¹Center for Integrated Nanotechnologies, Los Alamos National Laboratory, Los Alamos, NM, USA

²Materials Science and Technology, Los Alamos National Laboratory, Los Alamos, NM, USA

³Materials and Fuels Complex, Idaho National Laboratory, Idaho Falls, ID, USA

⁴George W. Woodruff School of Mechanical Engineering, Georgia Institute of Technology, Atlanta, GA, USA

⁵Center for Energy Research, University of California at San Diego, La Jolla, CA, USA

⁶Institute of Materials Science, Los Alamos National Laboratory, Los Alamos, NM, USA

⁷Chemical and Materials Engineering, University of Nevada, Reno, Reno, NV, USA

Received: 29 August 2017

Accepted: 15 November 2017

Published online:

19 December 2017

© Springer Science+Business Media, LLC, part of Springer Nature 2017

ABSTRACT

Recent advances in spherical nanoindentation protocols have proven very useful for capturing the grain-scale mechanical response of different metals. This is achieved by converting the load–displacement response into an effective indentation stress–strain response which reveals latent information such as the elastic–plastic transition or indentation yield strength and work-hardening behavior and subsequently correlating the response with the material structure (e.g., crystal orientation) at the indentation site. Using these protocols, we systematically study and quantify the microscale mechanical effects of He, W, and He + W ion irradiation on commercially pure, polycrystalline tungsten. The indentation stress–strain response is correlated with the crystal orientation from electron backscatter diffraction, the defect structure from transmission electron microscopy micrographs, and the stopping range of ions in matter calculations of displacement damage and He concentration. He-implanted grains show a much higher indentation yield strength and saturation stress compared to W-ion-irradiated grains for the same displacement damage. There is also good agreement between the dispersed barrier hardening model with a barrier strength of 0.5–0.8 and void models (Bacon–Kochs–Scattergood and Osetsky–Bacon models) with the experimentally observed changes in indentation strength due to the presence of He bubbles. This finding indicates that a high density ($\sim 9 \times 10^{23} \text{ m}^{-3}$) and concentration ($\sim 1.5 \text{ at.}\%$) of small ($\sim 1 \text{ nm}$ diameter) He bubbles can be moderate to strong barriers to dislocation slip in tungsten.

Address correspondence to E-mail: namara@lanl.gov; spathak@unr.edu

Introduction

Tungsten is one of the materials chosen for fusion reactors to protect other components from the high flux of thermal shock and high flux of particle bombardment (a.k.a. first wall material, plasma facing material, material for divertor) in addition to the high flux of neutron irradiation [1–5]. Hence, understanding and predicting how it will perform under the extreme conditions of a fusion reactor is important. Radiation damage by neutrons causes a number of types of crystalline defects (e.g., dislocation loops, helium bubbles) which lead to an increase in strength and loss in ductility and/or toughness [4, 6]. Besides atomic displacement damage in the tungsten lattice, the effect of helium, as a result of prolific helium production in tungsten by fast neutrons in the fusion environment, becomes a more significant radiation damage problem than in fission reactors [5]. Thus, understanding the effect of He as well as potential synergistic effects between displacement damage and He on the mechanical properties of tungsten becomes critically important.

Experiments approximating the effects of neutron radiation damage on material microstructure can be quickly performed with ion beam accelerators [6–8]. The irradiated material from ion beam experiments is typically to a depth on the order of a few microns or less which poses a significant challenge for mechanical testing. This requires small-scale mechanical testing such as nanoindentation, micropillar compression, and micro-cantilever beam bending (e.g., [8–15]). Micropillar compression and micro-cantilever beam bending protocols rely on focused ion beam (FIB) milling to fabricate nano-microscale specimens which entails a significant investment of time and specialized facilities. In contrast, nanoindentation is automated, high-throughput (many tests in a short period of time), and requires only a fraction of the investment of facilities. However, the typical approach of distilling nanoindentation tests into hardness and modulus measurements provides less prized information than a uniaxial stress–strain curve (e.g., from a micropillar compression or tension test). More valuable information potentially exists in nanoindentation tests, particularly when using spherical probes for which an effective stress–strain response can be determined from the measured load, displacement, and stiffness data [16–20]. The

protocols for extracting indentation stress–strain curves are rooted in the seminal works of Hertz [21, 22] and Tabor [23]. There have been many refinements in both the instrumentation and analyses for making indentation stress–strain measurements since Tabor's 1951 paper. Most notably, the protocol developed by Kalidindi and Pathak [18, 24, 25] has been shown to provide a physically meaningful effective stress–strain response by using robust strategies for the determination of the zero-point (initial contact) and the computation of indentation stress and strain measures. This protocol has been used successfully to study a variety of materials at multiple length scales [26–32].

The protocols for extracting material properties and/or model parameters from indentation stress–strain measurements for [18] have also been developed through modeling and inverse approaches [33–36]. The extraction of material properties from indentation stress–strain curves as opposed to indentation load–displacement curves is arguably a significant improvement in procedure since the initial elastic loading, elastic–plastic transition, and hardening behavior are clearly visible in the indentation stress–strain curve. This information is otherwise invisible in the load–displacement response making it difficult to evaluate the model accuracy through matching the load–displacement response. Recent work has also shown the potential of these indentation stress–strain protocols for characterizing structural gradients below the sample surface, specifically in He ion implanted tungsten [26].

This investigation extends the previous study [26] in an effort to answer some of the outstanding questions about the mechanical behavior of He irradiated tungsten: (1) What is the microstructure (types and morphology of defects) of the irradiated layer? (2) What are the roles of the different defects present in the resulting mechanical behavior of the material? (3) What is the effect of crystal orientation on the mechanical response of the irradiated material? These questions will be answered by systematically characterizing He, W, and He plus W (He + W) ion-irradiated polycrystalline tungsten through spherical nanoindentation of single grains and careful transmission electron microscopy (TEM) of the irradiated layer. Different hardening models will be explored to estimate the barrier strength of the primary defects in the irradiated layer from the experimental measurements obtained in this study.

Materials and methods

Commercially pure polycrystalline tungsten was annealed at 1500 °C for three days and metallographically prepared with a final step of electropolishing using a chilled sodium hydroxide solution at 8 V for 1 min. The average grain size of the sample measured by electron backscatter diffraction (EBSD) was 35 μm (grain size range 10–60 μm) [26]. Figure 1a shows the four regions of a single polycrystalline tungsten sample which were created by masking and subsequent ion beam irradiation. The annealed (e-polish) condition was characterized prior to ion beam irradiation; however, it also exists in one of the quadrants in the final sample for future characterization. He implantation was performed first, followed by W-ion irradiation creating regions with solely He and solely W irradiation and one region containing both He and W (first He and then W,

He + W) irradiation. Helium ion implantation and tungsten ion irradiation, both at room temperature, were performed on a 200 kV Danfysik Research Implanter and a 3MV Pelletron Tandem Ion Accelerator, respectively, at the Ion Beam Materials Laboratory (IBML) at Los Alamos National Laboratory (LANL). Multiple voltages and fluences were used to create a box-like profile of displacement damage of 0.5 dpa and He concentration of ~ 1.5 at.% starting from the highest energy: 200 keV at $2.0\text{E}16$ ions cm^{-2} , 150 keV at $4.0\text{E}15$ ions cm^{-2} , 100 keV at $8.0\text{E}15$ ions cm^{-2} , and 50 keV at $7.2\text{E}15$ ions cm^{-2} . The same box-like profile of displacement damage of 0.5 dpa was created for W irradiation starting from the lowest energy: 1.5 MeV at 1.3 ion cm^{-2} and 5 MeV at $6.2\text{E}13$ ions cm^{-2} . The SRIM [37] calculated damage and He concentration profiles are shown in Fig. 1d–f, where the full cascade mode along with the threshold displacement energy for W of 90 eV was used.

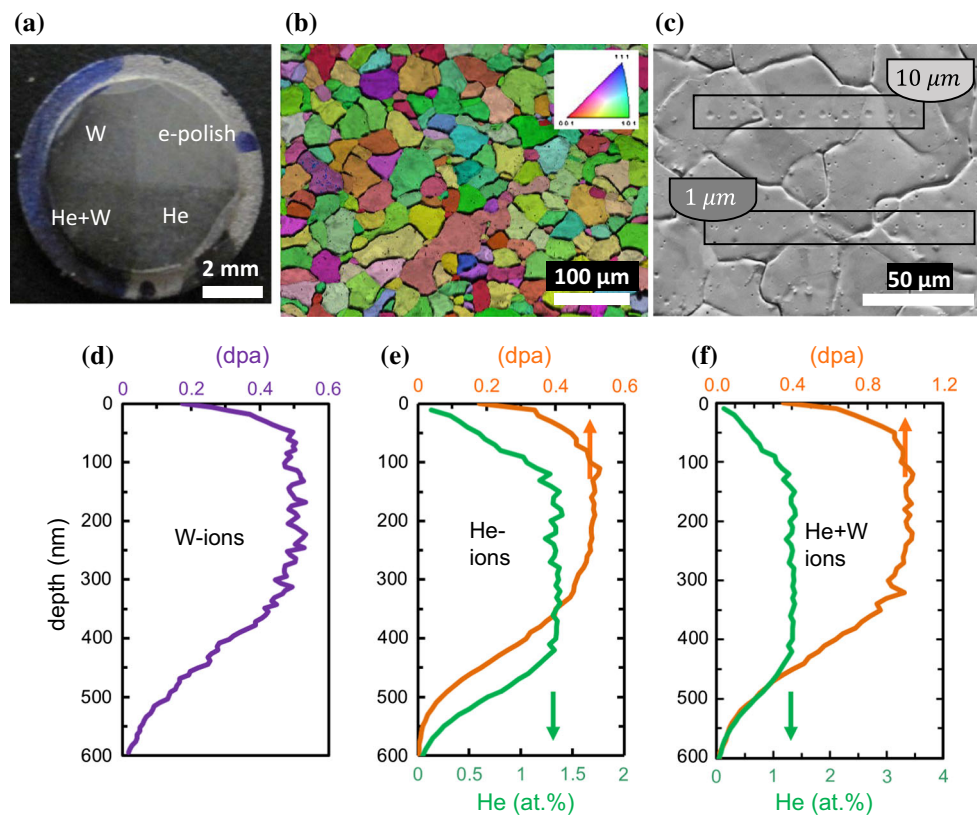


Figure 1 **a** Four quadrants of a polycrystalline tungsten sample which represent four different sample conditions: unirradiated (e-polish), He ion irradiated, W ion irradiated, and He followed by W (He + W) ion irradiated, **b** EBSD inverse pole figure plus image quality map of tungsten sample, **c** SEM micrograph of W sample with residual indents. Only indents inside grains away from grain

boundaries were considered., **d** SRIM calculated damage profile for W ions, **e** SRIM calculated damage profile and He concentration for He ions, **f** SRIM calculated damage and He concentration profiles for He + W ions. The profiles for He + W are the sum of He and W ion irradiation SRIM calculations.

Indentation was performed on an MTS XP Nano-Indenter with continuous stiffness measurement (CSM) in the Center for Integrated Nanotechnologies (CINT) at LANL. Sphero-conical diamond indenters with nominal tip radii of 1, 10, and 100 microns were used to characterize the material before and after irradiation. The use of spherical indenters with different radii presents an important advantage—to systematically study responses at different material volumetric or length scales by simply varying the indenter radii in order to study the heterogeneous damage gradient caused by irradiation. The 100- μm tip is particularly useful for determining the indentation strength of the annealed material because smaller indenter tips produce large pop-ins [32, 38–40]. The 1 and 10 micron radius tips were useful for determining the local strength of the irradiated material at different depths corresponding approximately to about 1/10–1/20 of the indenter tip radius. This is especially important since the irradiated layer thickness was limited to about 0.5 μm . A constant loading rate divided by the load of 0.05 s^{-1} was used to a maximum indentation depth of $\sim 300 \text{ nm}$ for all indenter sizes. CSM was obtained at 2 nm displacement amplitude and 45 Hz. Arrays of indents were carefully placed inside grains as shown in Fig. 1c. Indents that fell too close to grain boundaries were ignored. The load (P), displacement (h), and CSM stiffness (S) were converted to indentation stress (σ_{ind}) and indentation strain (ε_{ind}) according to Eqs. (1–3) [18] where the contact radius (a) is determined from the CSM stiffness and the effective modulus (E_{eff}). See the supplemental material for more details.

$$\sigma_{\text{ind}} = \frac{P}{\pi a^2} \quad (1)$$

$$\varepsilon_{\text{ind}} = \frac{4}{3\pi} \frac{h}{a} \quad (2)$$

$$a = \frac{S}{2E_{\text{eff}}} \quad (3)$$

Additionally a diamond Berkovich (pyramidal) tip was used to indent up to a depth of 600 nm. The same method was used: strain rate of 0.05 s^{-1} with CSM at 2 nm displacement amplitude and 45 Hz frequency. The tip area function and frame stiffness were calibrated from indents on fused silica up to 2,000 nm displacement, and the modulus and hardness were determined in accordance with the Oliver–

Pharr method [41]. A Poisson's ratio of 0.3 was assumed for tungsten in the calculation of Young's modulus from nanoindentation data.

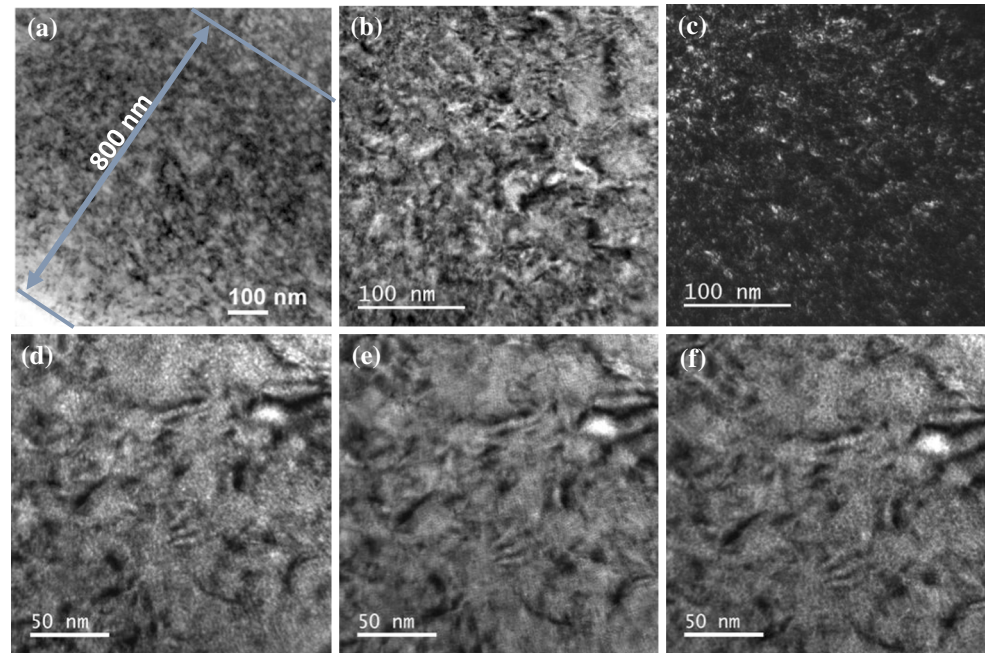
SEM (FEI XL30 and Inspect microscopes) and EBSD (EDAX Digiview camera) were used to place indents and confirm their locations (indentation site orientation). TEM (FEI Tecnai F30) was used to observe and quantify the defects in the irradiated layer. Figure 2 shows representative TEM micrographs of the dislocation loops and He bubbles in the irradiated layer for the He + W region. The apparent depth of damage goes to approximately 800 nm; the uniform damaged region is between 200 and 700 nm, and the He bubbles end at a depth of $\sim 500 \text{ nm}$. This is slightly deeper than the SRIM calculated profiles in Fig. 1d–f. In the uniformly damaged region, the helium bubble density and diameter determined in the underfocus imaging condition [42] were $\sim 8.5 \times 10^{23} \text{ m}^{-3}$ and $\sim 1.1 \text{ nm}$ for He-implanted tungsten (He) and $\sim 9.1 \times 10^{23} \text{ m}^{-3}$ and $\sim 1.1 \text{ nm}$ for He-implanted and W-irradiated tungsten (He + W). Thus, the He bubble size and density did not change significantly between the He-implanted and He + W regions. The average dislocation loop density and diameter were determined to be $\sim 3 \times 10^{23} \text{ m}^{-3}$ and $\sim 3 \text{ nm}$ on the He + W region. These dislocation loops have $\frac{1}{2}111\{110\}$ character. TEM foil thickness was measured by electron energy loss spectroscopy (EELS). Dislocation loops could be seen in the He-implanted region as well, and we assume they are also present in the W-irradiated region. However, they were not quantified in these regions. It will be shown later that the dominant defect on the indentation response is from the He bubbles for these irradiation conditions.

Theory

Physical interpretation of indentation stress–strain measurements

The indentation stress–strain response is highly sensitive to the salient attributes of the averaged structure in the indentation zone such as the crystal orientation, dislocation density. The crystal orientation plays an important role due to the orientation of slip systems with respect to the loading direction in both cubic [28, 32] and hexagonal [27, 29] crystals. After accounting for crystal orientation effects, an

Figure 2 TEM micrographs on He-implanted and W-irradiated W (He + W). **a** Showing the distribution of dislocation loops across the damaged region. The uniform damaged region is a depth between 200 and 700 nm. **b–c** bright and dark field images showing evidence of dislocation loops. **d–f** under focused, in-focus, and over focused images showing He bubbles. He bubbles end at a depth of ~ 500 nm.



increase in the indentation yield strength between an annealed sample and a deformed or irradiated sample can be attributed to changes in the defect density (e.g., dislocation density) in the deformed or irradiated sample [28, 32]. In prior work, it was demonstrated that the indentation yield strength measurement is sensitive enough to capture the dislocation density differences in grain boundary regions compared to in-grain regions in plastically deformed samples [43, 44].

In cubic metals, it is reasonable to assume a single value of slip resistance for all slip systems operating in the indentation zone. With this simplification, the equations relating changes in the critical resolved shear stress, τ_{crss} , to changes in the indentation yield strength, Y_{ind} , and dislocation density, ρ , can be expressed as follows:

$$Y_{\text{ind}}(g, d) = M(g)\tau_{\text{crss}}(d) \quad (4)$$

$$\Delta\tau_{\text{crss}} = \tau_{\text{crss}}(d) - \tau_{\text{crss}}(0) \propto \sqrt{\rho} \quad (5)$$

$$\Delta Y_{\text{ind}}(g, d) = Y_{\text{ind}}(g, d) - Y_{\text{ind}}(g, 0) = M(g)\Delta\tau_{\text{crss}} \quad (6)$$

where g is the crystal orientation, d represents some amount of bulk deformation, and M is similar to a Taylor factor for indentation. Since the indentation Taylor factor is not easily computed (needs a sophisticated finite element simulation of indentation using crystal plasticity theories), a percentage change in indentation yield strength or critical resolved shear stress has been reported in previous studies

[28, 32, 44, 45]. The equations presented above will be used in this work for interpreting changes in indentation yield strength in irradiated materials. In the present work, d would represent an irradiation dose rather than bulk deformation. For irradiated materials, there are also various models to estimate τ_{crss} for different types of defects, which would modify Eq. (5). These are described in Sect. 3.2.

It is helpful to try to establish relationships between indentation and uniaxial tests so that indentation testing can be used as a surrogate to uniaxial testing. Our understanding of the static mechanical behavior of most materials is primarily based on uniaxial stress–strain curves. There is inherently some uncertainty in converting indentation properties to uniaxial properties (e.g., strength) because the deformation processes are very different. One can only seek to reduce this uncertainty through rigorous protocols. It is common practice to measure hardness and convert to uniaxial yield strength by dividing by a factor of ~ 3 [46, 47]. The factor can be more precisely determined through careful experiments or simulations for a particular class of materials (e.g., [48]); however, there is a high degree of uncertainty in this practice. This is due to the fact that hardness corresponds to a plastic flow stress well past the yield point. Thus, converting hardness to uniaxial yield strength requires an extrapolation over a potentially large section of the material response. It

is wiser to try to establish the indentation stress at the early stage of plastic deformation under the indenter and relate this to uniaxial yield strength. This has been done with simulations [33, 35] and experiments [30] using the indentation stress–strain protocols described in section [18]. For isotropic materials whose plasticity can be described by J_2 flow theory, the indentation yield strength, Y_{ind} , is approximately twice the uniaxial yield strength, σ_{ys} , [33].

$$Y_{\text{ind}} = \sim 2.0 * \sigma_{ys} \quad (7)$$

More work is required to develop the theory for anisotropic materials and more complex material models [15, 49]; however, experiments show that the isotropic factor of 2 is still a reasonable approximation for more complex materials [31].

One final consideration must be made in interpreting the indentation stress–strain response: the indenter size effect (ISE). For spherical indenters, the ISE refers to (1) discrete displacement or strain bursts (for a load-controlled test) at low indentation depths, more commonly known as pop-ins in nanoindentation, and (2) an apparent increase in the indentation stress (i.e., hardness) as the indenter radius decreases, a ‘smaller is stronger’ effect. Unlike sharp pyramidal indenters (e.g., Berkovich and cube corner) [50], pop-ins for spherical indenters are manifested not through the depth of penetration but rather through the radius of the sphere [51]. Thus, large pop-ins have been observed for smaller indenter radii, with the pop-in size decreasing for larger indenters [52]. Our results show a similar trend (Figs. 3 and 4 and Ref. [26]). In our tests on annealed tungsten, the largest indentation strain burst is seen for the smaller indenter tip radii of 1 μm ; the burst size decreases for larger 10 μm indenter radius, while the pop-in completely disappears for the largest 100 μm indenter radius [53, 54]. Note that none of the measurements in the irradiated sample revealed any pop-ins. This effect is discussed later.

Many studies have also reported a second ISE for spherical indenters [50–52, 55, 56] where the refrain ‘smaller is stronger’ holds true (i.e., the indentation stresses appear to increase as the indenter radius decreases). The indentation stress–strain protocols employed in this work have not shown any evidence of an indenter size effect on the indentation yield strength of single grains for metals that deform primarily by slip [29, 32, 57]. Similar trends showing a consistent indentation stress–strain response for

indenters of different sizes have also been reported by others [58]. The definition of indentation yield strength is such that it disregards pop-in events which clearly show a dependence on the indenter size [38–40]. This is because the goal is to measure the strength of a small volume of material that is not dislocation starved. More precisely, if a large pop-in occurs, the indentation yield strength cannot be reliably determined; however, for small pop-ins, the indentation yield strength can be determined from back-extrapolating the portion of stress–strain response after the pop-in event to a 0.2% strain offset [29, 32, 57]. Indentation work hardening has been less rigorously studied, and it is not clear what the effects of indenter size are, particularly in deformed materials [32, 57]. Once a significant volume of material under the indenter yields, the effect of the strain gradient (possible cause for indentation and indenter size effects on hardness [50, 51, 55, 56]) may become more prevalent. Phase transformation and twinning are additional deformation mechanisms known to show size effects; and these have been observed in indentation experiments [27, 59, 60]. However, these do not occur in tungsten at room temperature under the imposed loading conditions which deforms by dislocation slip. Thus, in this work we can freely compare indentation strength measurements from different indenter sizes (1–100 μm radii) inside single grains as long as pop-ins do not obscure the indentation yield point. More specifically, the indentation yield strength on the annealed tungsten is determined from a 100- μm -radius tip in order to measure the strength at a length scale that is not dislocation starved, and 1–10- μm -radii tips are used to measure the strength of the irradiated layer. The irradiated layer is not dislocation starved even for the smallest tip due to the high density of dislocation sources after radiation damage and requires smaller tip sizes in order to separate out the response of the irradiated layer from the unirradiated material below. The ISE on the indentation yield strengths observed in the irradiated material in this work will be shown to primarily relate to the structure (e.g., depth of damage) of the irradiated layer.

Hardening models for radiation damage

Various models exist to predict the critical resolved shear stress, τ , required for plastic deformation for different types of defects, which are typically

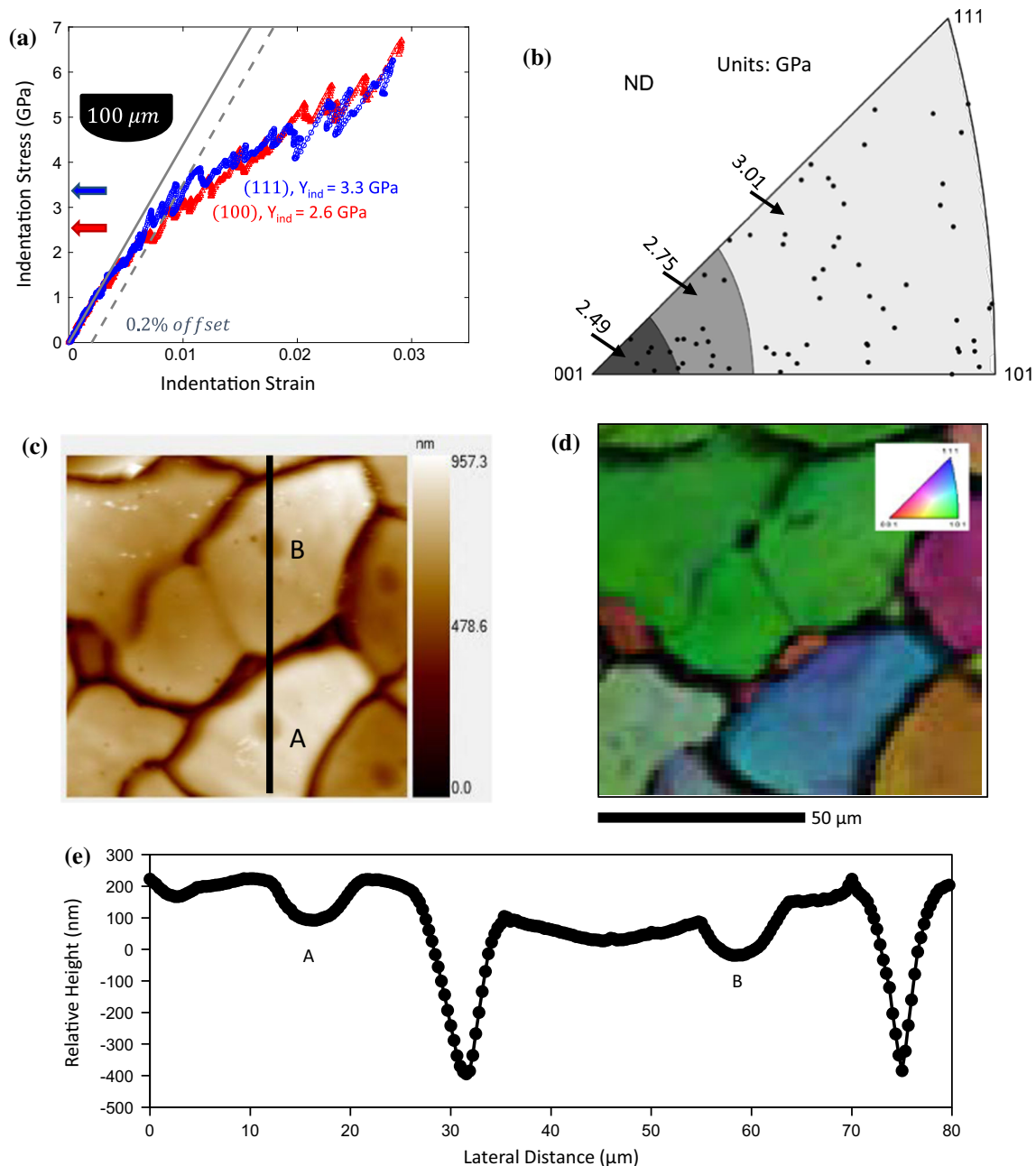


Figure 3 **a** Representative indentation stress–strain curves for 100- μm indenter on annealed tungsten for grains with normal directions near (100) and (111) crystal directions. **b** The best fit representation of the orientation dependence for 100- μm -radius indenter stress–strain response as an IPF contour map. Each black

point is a grain with 1–2 tests. **c–d** Depth contour map from low force scanning with Berkovich tip after an average plane background correction and corresponding IPF-IQ map. **e** Relative depth profile along highlighted line across two grain boundaries and indents.

determined by calculating the force required to move a perfect line defect through an array of defects. Four models, with varying sets of assumptions, are used here to predict the increase in slip resistance due to defects caused by radiation damage: the dispersed barrier hardening (DBH) model [61], the Friedel–

Kroupa–Hirsch (FKH) model [62, 63], the Bacon–Kocks–Scattergood (BKS) model [64, 65], and the recent work by Osetsky and Bacon (OB) [66]. These are expressed below:

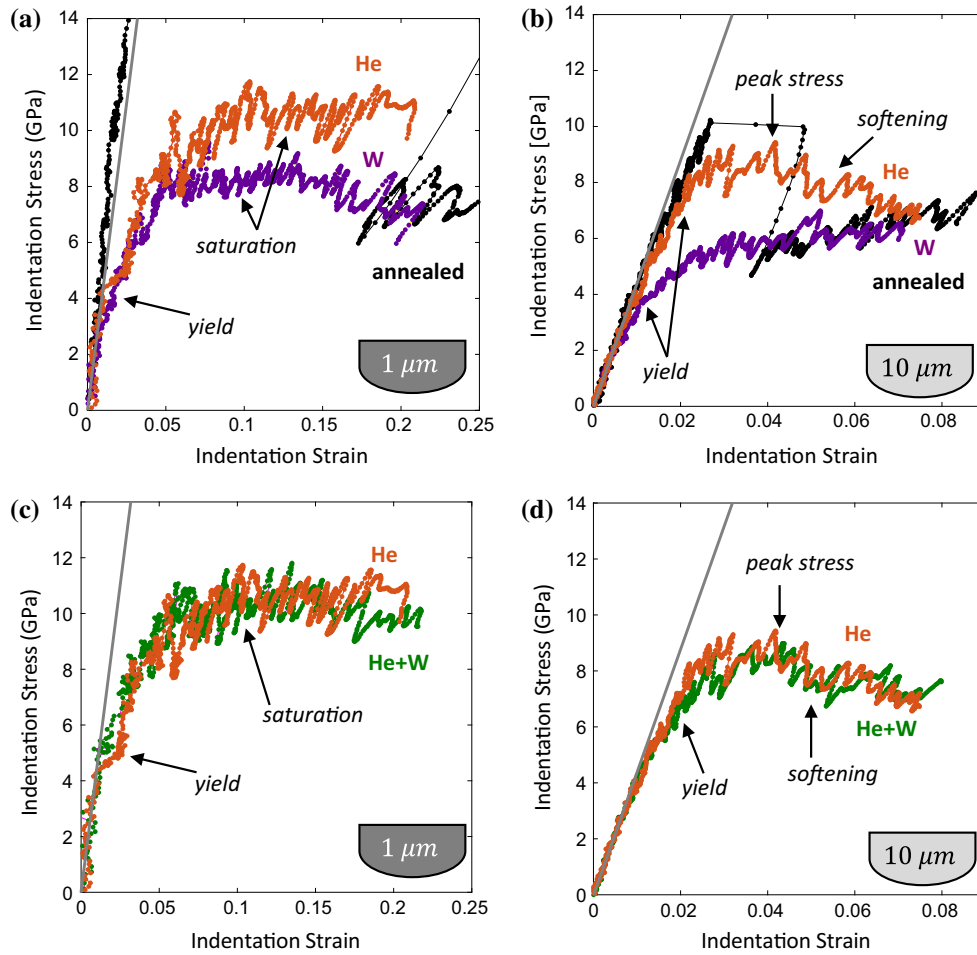


Figure 4 Representative indentation stress–strain curves for two different indenter sizes and four different conditions: **a** 1- μm -radius indenter for annealed unirradiated, He ion irradiated, and W ion irradiated. **b** 10- μm -radius indenter for annealed unirradiated, He ion irradiated, and W ion irradiated. **c** 1- μm -radius indenter for He ion irradiated and He + W ions irradiated. **d** 10- μm -radius

indenter for He ion irradiated and He + W ions irradiated. All orientations are near (100) direction so as to remove any orientation effects from the comparisons. The modulus line represents the indentation modulus using a Young’s modulus of 405 GPa and a Poisson’s ratio of 0.28 (i.e., $E_{\text{ind}} = 405 / (1 - 0.28^2) = 439$ GPa).

$$\tau_{\text{DBH}} = \frac{\alpha \mu b}{L} \tag{8}$$

$$\tau_{\text{FKH}} = \frac{\mu b^0 D N^{\frac{2}{3}}}{16} \tag{9}$$

$$\tau_{\text{BKS}} = \frac{\mu b}{2\pi L} \left[\ln\left(\frac{L}{r_0}\right) \right]^{-\frac{1}{2}} \left[\ln\left(\frac{1}{(D^{-1} + L^{-1})r_0}\right) + 0.7 \right]^{\frac{3}{2}} \tag{10}$$

$$\tau_{\text{OB}} = \frac{\mu b}{2\pi L} \left[\ln\left(\frac{1}{(D^{-1} + L^{-1})r_0}\right) + \Delta \right] \tag{11}$$

where μ is the shear modulus, b is the glide dislocation Burgers vector magnitude, b^0 is the circular prismatic loop Burgers vector magnitude (in this case

b and b^0 are the same $\frac{1}{2}111 = 0.274\text{nm}$), N is the density of the defect, D is the average diameter of the defect, L is the average defect spacing, and r_0 is the cutoff or dislocation core radius. For simplicity, in this work, the average defect spacing is determined from the average diameter and density as $L = 1/\sqrt{ND}$. The core radius for an edge dislocation can be determined as $r_0 = \frac{b}{2} \exp\left(\frac{1-2\nu}{4(1-\nu)}\right)$ where ν is the Poisson’s ratio [67]. The DBH and OS models have empirical factors which vary based on the defect type [66, 68]. The barrier strength in Eq. (8), α : $0 < \alpha \leq 1$, takes a value of 1 for an impenetrable barrier. The

empirical factor in Eq. (10) is $\Delta = 0.77$ for Orowan hardening and $\Delta = 1.52$ for voids [66].

Since the indentation Taylor factor in Eq. (4) cannot be easily calculated, the shear strengths from Eqs. (8–11) are converted to uniaxial strengths using an average uniaxial Taylor factor of $M = 3.06$ ($\sigma_{ys} = M\tau_{crss}$). Equation (7) can then be used to convert the predicted uniaxial strengths to indentation yield strengths. Note that these predictions are not grain-scale predictions since the conversion factors (Taylor and constraint factors) used are for an average crystal or isotropic response. Thus, the predictions will be compared with the average (over many orientations) response. We are also assuming that the defect densities for the defects generated during irradiation were zero or insignificant in the starting material. A simple superposition rule ($\Delta\tau_{total} = \sqrt{\Delta\tau_A^2 + \Delta\tau_B^2}$) summing the contributions of each $\Delta\tau$ will be used [65, 69] for the combined effect of two types of defects.

Results

Indentation stress–strain response of annealed condition

Representative indentation stress–strain curves obtained on the annealed sample using a 100- μm -radius indenter are shown in Fig. 3a. As mentioned earlier, the larger indenter size is required to avoid large pop-in events, which obscure the determination of the indentation yield point. Note that this information is critically needed for the interpretation of the indentation measurements on the irradiated samples. There is a measurable difference in the indentation yield strengths in the annealed sample between grains near (100) orientation and (111) orientation ($\sim 27\%$ increase); however, the difference in response at larger strains becomes almost indistinguishable. The measured trend in the indentation yield strength with crystal orientation is shown as an inverse pole figure contour plot, Fig. 3b. The trend in indentation yield strength is similar to that reported in Fe–3%Si [28]; however, the variance between grains with similar orientations is quite large compared to the average trend. For example, grains with crystal directions within ~ 10 degrees of the (100), (101), and (111) poles have average indentation

strengths of 2.69 ± 0.15 , 3.21 ± 0.22 , 3.00 ± 0.22 GPa, respectively. The number of grains tested (one test per grain) near each pole was 7, 9, and 4, respectively. It is believed that the large variance for similar orientations and the overlapping response at higher strains for different orientations are due to the relatively large indenter size compared to the grain size. The average contact diameters (width of the primary indentation zone) at yield and at a strain offset of 1% are ~ 2.4 and ~ 5 μm , respectively, compared to the average grain size of 35 μm . This means there is a high chance of having some tests with grain neighbors influencing the response due to grain boundaries which run close to parallel with the surface and/or grains which end at shallow depths (< 5 μm) below the surface. The electropolishing also preferentially etches the grain boundaries as shown in Fig. 3c and e. This creates even less area with a flat surface for 100- μm indents. More profiles of Fig. 3c are shown in the supplementary information which further illustrates this point. In fact about 75% of tests using the 100- μm indenter were discarded for landing too close to grain boundaries, poor initial contact due to unknown surface disparities (e.g., curvature, roughness), machine error, sudden changes in slope in the load–displacement curve, etc. For these reasons, there is a high degree of uncertainty, represented by the standard deviation, in the indentation yield strength, and even greater skepticism in the post yield response (overlapping response for (100) and (111) crystals). However, we are fairly confident in the trend and averages in the indentation yield strength since a large number of measurements (69 tests) were made, and there is good agreement with the trend for α -Fe [28]. These indentation strength measurements will be used to describe the unirradiated indentation strength for comparison with irradiated regions.

Effect of ion species on the indentation stress–strain response

Since the irradiated layer is limited to the first 800 nm of the sample, 1–10- μm -radius indenters are required to determine the indentation properties of the ion-damaged region. This was demonstrated in our previous work (Pathak et al. [26]) for the He-implanted tungsten region. Figure 4 shows representative indentation stress–strain curves for 1- and 10- μm -radius indenters for all four regions for grains close to

the (100) crystal direction. The y-axis of Fig. 4a is purposely chosen to focus on the irradiated condition and not the pop-in which has been cutoff in this plot. There are four important observations that can be made from Fig. 4: (1) He-implanted tungsten exhibits higher plastic flow strengths compared to W-irradiated tungsten, (2) there is no significant difference between the indentation response of the He and He + W regions despite twice the dpa damage for the He + W compared to the He region, (3) the 1- μm indenter response is very similar for all irradiated conditions up to $\sim 5\%$ indentation strain, (4) 1- and 10- μm indenters show different responses for the same irradiated material, and (5) pop-ins are no longer prevalent in the irradiated material. Each of these is discussed in more detail below.

First, helium-implanted tungsten (He) exhibits higher plastic flow strengths compared to tungsten irradiated tungsten (W). This conclusion is reached by comparing the saturation indentation stresses in the 1- μm indenter test and the indentation yield strengths in the 10- μm indenter test. This is despite the fact that these two regions exhibited the same SRIM calculated displacement damage. This observation suggests that He bubbles play a more dominant role in the mechanical response compared to just dislocation loops. Qualitatively similar results have been seen in Refs. [12, 70], where hardness increases resulting from He implantation into tungsten were more pronounced than self-ion or Fe^{3+} ion irradiations.

Second, indentation tests in He-implanted, W-irradiated (He + W) region show the same response as the He-implanted (He) region. This is surprising given the fact that the dpa damage across all depths is two times higher at ~ 1.0 dpa in the He + W region compared to the ~ 0.5 dpa in the He region. TEM showed that the bubble size and densities are identical in the two regions meaning that the additional 0.5 dpa from W ions following 0.5 dpa from He ions did not affect the He bubble barrier strength. Rather the additional 0.5 dpa likely changed the dislocation loop morphology, increasing the loop density. Thus, small changes in dislocation loop morphology after He implantation appear to have little effect on the indentation response.

Third, the 1- μm indenter response is very similar for all irradiated conditions up to $\sim 5\%$ indentation strain. In order to understand this observation, the structure of the irradiated layer must be carefully

considered in conjunction with the primary indentation zone as suggested by Pathak et al. [26]. The primary indentation zone is approximated as a cylinder with diameter of two times the contact radius and height of 2.4 times the contact radius. This zone represents the volume where most of the stress and strain imposed by the indenter is contained [18, 35]. For all 1- μm indenter tests on the irradiated regions, the contact radius at yield was ~ 30 nm; the contact radius at strain offsets (using the indentation modulus) of 2, 6, and 15% indentation strain was ~ 40 , 100, and 400 nm, respectively. As seen from the SRIM calculated He concentration profile in Fig. 1e and f, there is less He in the first 100 nm of depth of the transition region as compared to the uniformly irradiated layer where the He concentration in tungsten was estimated to be the highest (100–400 nm depth). Given the surface effect on interstitial migration, it is rather difficult to reliably measure the differences in He content in the first 100 nm. Thus, we will rely on the SRIM calculated profile (less He concentration in the first 50 nm of depth) to infer that the implanted He inside the primary indentation zone up to a 2% indentation strain offset does not contribute significantly to the mechanical response. This would explain why the 1- μm indentation stress–strain curves behave nearly the same for all irradiated conditions up to a 2% indentation strain offset. Once the primary indentation zone spills into the constant irradiated layer (6% indentation strain offset) and constant He concentrated layer, the responses of He-implanted regions (He and He + W) separate from just W-irradiated tungsten (W). The primary indentation zone up to an indentation strain offset of 15% is mainly within the constant irradiated layer.

Fourth, the 10- μm indenter response shows differences from the 1- μm indenter response for the same irradiated material which can again be explained by considering the evolution of the primary indentation zone (contact radius) with respect to the structure of the irradiated layer. For example, the 10- μm indents on He-implanted regions (He and He + W) have higher indentation yield strengths (~ 6 GPa) than their counterpart 1 μm tests (~ 4.25 GPa). This suggests that the indentation zone for the 10- μm indents at yield experiences a larger concentration of He-based obstacles to plasticity than the 1- μm indents. This is also evident from the contact radius at yield for the 10- μm indents, which is around 300 nm and

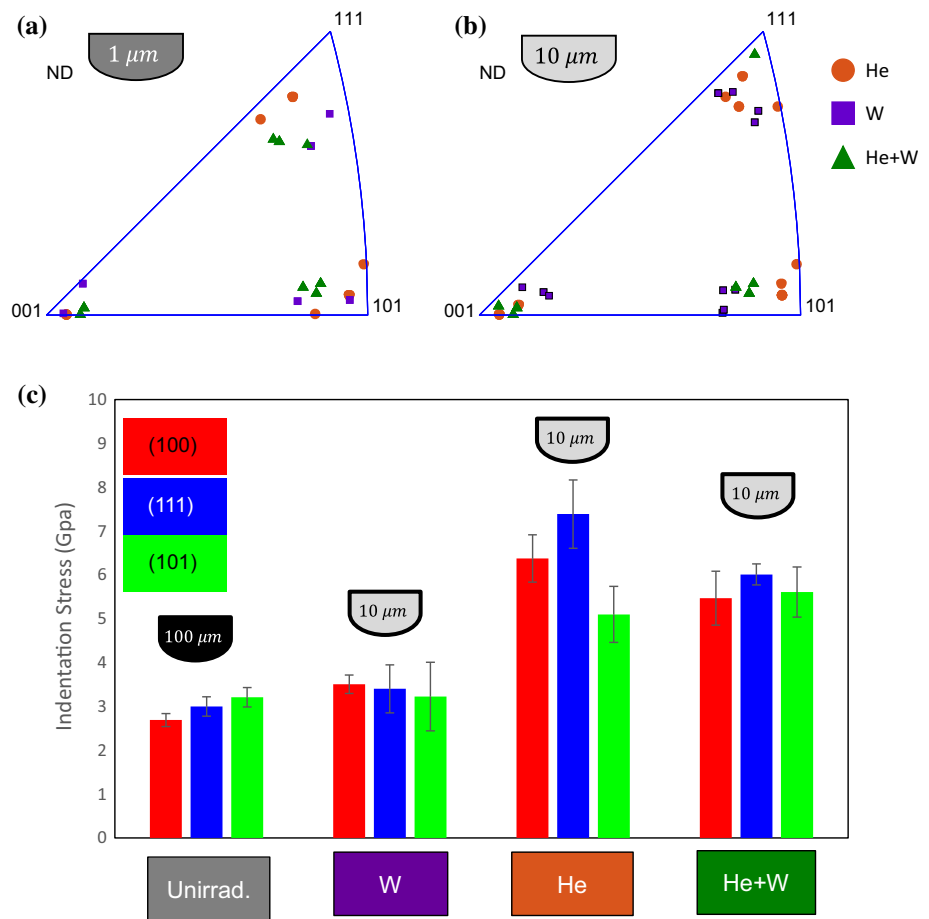
well within the region of constant-dpa and He concentration. This is further evidence that the depleted region in the He concentration profile in the first 50 nm is important to consider in interpreting the response. At larger indentation strains, softening occurs in the 10 μm radius indenter response of the He irradiated regions (He and He + W) that does not occur in the 1- μm -radius indenter tests. This softening occurs in the 10 μm radius tests at a strain offset of $\sim 2\%$ and contact radius of 575 nm. Clearly from SRIM and TEM, the primary indentation zone has spilled into He-free material and eventually damage-free material (> 800 nm). The contact radius at the end of the tests is ~ 1.4 μm . It therefore makes sense that the indentation stress would drop since this material (unirradiated) is not as hard as the irradiated layers. Similar strain softening has been reported by others for tests using spherical indenters [58].

Last, it is clear that the pop-ins that were prevalent in the unirradiated (annealed) material have disappeared. There may be some small pop-in events for the 1- μm indenter in the W-irradiated tungsten (W) case, but their size is significantly reduced to the point that it is difficult to clearly identify them as pop-ins. No pop-ins were observed for all 10- μm indenter tests on W-irradiated tungsten and for 1- and 10- μm indenter tests on the He-implanted regions (He and He + W). The general understanding of pop-in events during nanoindentation in metals (which do not twin or have stress/strain-induced phase transformations) is that they relate to the difficulty or ease of activating a dislocation source in the volume of material probed [38–40, 71, 72]. It is possible to probe volumes that are starved of sources with small indenter tips, and the stress required to generate a source can be very high even approaching the theoretical shear stress for a perfect crystal [38–40]. In the irradiated material, there are plenty of ion-implantation-generated defects (dislocation loops and He bubbles) which can potentially serve to activate dislocation sources eliminating the need to generate a source, as reported by numerous indentation studies on ion-irradiated materials [13, 70, 73, 74]. Thus, it is not surprising that there are practically no pop-ins in the irradiated material.

Crystal orientation effects on the indentation stress–strain response of the irradiated material

One of the advantages of spherical nanoindentation protocols is that many grain orientations can be tested in a high-throughput manner. As discussed earlier, these experiments are analogous to single crystal experiments; however, the stress and strain under the indenter is highly heterogeneous. In spite of this heterogeneity, the indentation response shows a strong dependence on the grain orientation in cubic and hexagonal metals (discussed in Sect. 3.1). This was seen in the indentation yield strength measurements in the unirradiated (annealed) material despite the difficulty in making reliable measurements on small grains (relative to the indenter size). This difficulty is significantly mitigated with the 10- and 1- μm -radius indenters because the contact radii are significantly smaller than the 100 μm tests and grain sizes. Figure 5 shows the grain orientations that were tested for each irradiated region for two indenter sizes (1 and 10 μm radii) that were near the three poles (i.e., (100), (101), and (111)) in the inverse pole figure. The average indentation yield strength (0.2% offset) values are also shown in Fig. 5. The orientation trend for the indentation yield strength ($Y_{\text{ind}}^{(100)} < Y_{\text{ind}}^{(111)} \cong Y_{\text{ind}}^{(101)}$) present in the unirradiated material is no longer apparent in the irradiated material. This is true for other definitions of indentation stress (i.e., 10 μm peak stress, 1 μm saturation stress). Representative indentation stress–strain curves for each pole are shown in the supplementary information which also show that the stress–strain response for each indenter size and irradiated region are indistinguishable. The irradiated material appears to behave more plastically isotropic than the unirradiated material. There is a level of uncertainty in this observation as seen by the large error bars in most cases. These error bars relate both to the large spread of orientations seen in the IPF maps (Figs. 5b, c) as well as the inherent scatter of the nanoindentation measurements. In other words, some orientation trend could exist that would be unresolvable because of the variance in the measurements. Additional work is clearly required to study the grain orientation effects in the irradiated samples.

Figure 5 Grain orientations tested in the form of inverse pole figures for different irradiated conditions for **a** 1- μm indenter and **b** 10- μm indenter. **c** The average indentation yield strengths (0.2% offset) for annealed and irradiated conditions for grain orientations near (100), (101), and (111) poles.



Hardening predictions for He bubbles and dislocation loops

One of the main goals of this study was to investigate mechanical response of tungsten to a high fluence of implanted He with respect to the displacement damage particularly important for fusion reactor materials. In these experiments, we want to know the plastic flow strength of the constant irradiated/implanted region. For this goal, the He-depleted region < 50 nm presents a challenge. Reliably removing this top layer would be challenging without inducing additional damage (e.g., chemical, ion, mechanical). Therefore, there is some uncertainty in the measured indentation strength of the constant irradiated/implanted region. We will assume the bounded estimates for the constant He-implanted layer strength are given by the 0.2% strain offset indentation yield strength from the 10- μm indenter tests (possibly under estimates due to the top depleted layer) and the saturation stress from 1- μm indenter tests (possibly overestimates if the material significantly work

hardens). The strength of the W-irradiated tungsten region is less affected by the diminished displacement damage region at the surface (similar yield strengths for 1- and 10- μm -radius indenters); however, we will use the same measurement strategy to describe the estimated bounds for its plastic flow strength for now and attempt to understand which one is a better choice.

The strength measurements for all four regions averaged over all three orientation groups (near (100), (101), and (111)) are listed in Table 1. Using the equations in Sect. 3 with the measurements from TEM, the predicted increase in the indentation strength, ΔY_{ind} , of the irradiated materials is compared graphically against indentation strength measurements in Fig. 6. This comparison is broken up into two cases: dislocation loops (W-irradiated region, Fig. 6a) and He bubbles (He-implanted and He + W regions, Fig. 6b). The predictions for the W-irradiated region are based on the dislocation loop measurements for the He + W region (density of $3 \times 10^{23} \text{ m}^{-3}$ and diameter of 3 nm). The actual

Table 1 Indentation strength measurements averaged over near (100), (101), and (111) grains for all indenter sizes and irradiated regions. ΔY_{ind} is calculated as the difference between each condition-indenter size and the unirradiated, 100- μm -radius indenter yield strength (e.g., $\Delta Y_{\text{ind}} = Y_{\text{ind}}(W, 1 \mu\text{m}, \text{saturation}) - Y_{\text{ind}}(\text{unirradiated}, 100 \mu\text{m}, 0.2\% \text{ offset}) = 8.23 - 2.97 = 5.26 \text{ GPa}$)

Irradiated region	Indenter size (μm)	Definition	Y_{ind} (GPa)	Std.	ΔY_{ind} (GPa)	Std.
Unirradiated	100	0.2% offset	2.97	0.34	n/a	n/a
W	1	0.2% offset	3.93	1.44	0.96	1.48
He	1	0.2% offset	4.45	1.39	1.48	0.17
He + W	1	0.2% offset	4.87	2.36	1.90	2.38
W	1	Saturation	8.23	2.57	5.26	2.6
He	1	Saturation	10.27	0.97	7.30	1.03
He + W	1	Saturation	10.26	1.74	7.29	1.78
W	10	0.2% offset	3.38	0.98	0.41	1.03
He	10	0.2% offset	6.29	1.14	3.32	1.20
He + W	10	0.2% offset	5.70	0.87	2.73	0.94
W	10	Peak stress	n/a	n/a	n/a	n/a
He	10	Peak stress	9.02	1.02	6.05	1.07
He + W	10	Peak stress	8.48	0.64	5.51	0.72

density in the W-irradiated region is likely less since it has half the displacement damage of the He + W, but the loop measurements are still a good approximation. The measurements for He and He + W are shown on the same plot (Fig. 6b) since there was no significant difference between them. In Fig. 6b, two predictions are calculated to compare with He and He + W indentation measurements: one using only the He bubbles (density of $9.0 \times 10^{23} \text{ m}^{-3}$ and diameter of 1.1 nm) ignoring the contribution from dislocation loops and one using a superposition of He bubbles and dislocation loops using the loop measurements for the He + W region (density of $3 \times 10^{23} \text{ m}^{-3}$ and diameter of 3 nm). It is clear that the dislocation loops do not play a significant role in the change in indentation yield stress due to their lower density, slightly larger size, and lower barrier strength compared to the He bubbles.

Figure 6 can be used to determine which indentation stress measurements (i.e., 10 μm radius 0.2% yield point, 10- μm -radius peak stress, 1- μm -radius saturation stress) and hardening models are more approximate for the different irradiated regions/defects. For the first case (Fig. 6a), just dislocation loops, it becomes pretty clear that the 1 μm saturation stress (listed in Table 1) is an unreasonable measure of the constant irradiated layer strength because it far exceeds any reasonable predictions. In other words, the stress reflects a significant amount of work hardening. Thus, it was not included in Fig. 6a. Using the 1 and 10 μm indentation 0.2% yield strengths, the DBH model with a weak to moderate barrier strength

coefficient ($\alpha = 0.1\text{--}0.3$) provides an estimate close to the average. This barrier strength coefficient is reasonable based on the reported values in the literature [68, 75]. It is difficult to rule out or select the best model since all the predictions are within the error bars of the measurements. For He bubbles (Fig. 6b), it is less clear if the 1 μm saturation stress or 10 μm 0.2% yield strength is a better measure of the constant implanted/irradiated region. Therefore, both will be used as bounds (the true value is likely to lie somewhere between them). It is clear that the FKH model can be definitively eliminated for predicting the increase in indentation yield strength for He bubbles in these experiments, while the DBH model ($\alpha = 0.5$) and OB model for voids ($\Delta = 1.52$) provide estimates closest to the middle of the range.

Discussion

The primary observation from Figs. 4, 5 and 6 was that the He-implanted tungsten had higher plastic flow strengths than W-irradiated tungsten for the same displacement damage, and He-implanted tungsten had the same plastic flow strengths as He + W-irradiated tungsten for the same displacement damage. The discussion below is aimed at understanding these results by exploring different hardening models which provide predictions based on the defect types/barrier strengths and morphologies. These are undoubtedly different for He bubbles and dislocation loops and likely the reason for the

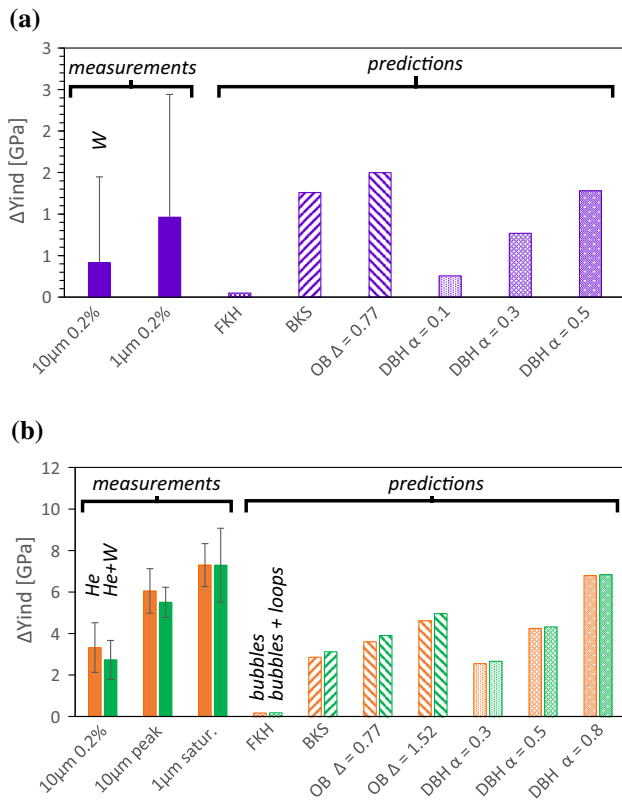


Figure 6 Predicted changes in indentation yield strength for different models and the indentation strength measurements from experiments for **a** W-irradiated tungsten and **b** He and He + W-irradiated tungsten. The empirical factor for the loops was equal to the bubbles for the OB superposition prediction, and the empirical factor listed for the DBH prediction corresponds to the bubbles only. (A value of 0.3 was used for loops in these cases.) ΔY_{ind} is calculated as the difference between each condition-indenter size and the unirradiated, 100- μ m-radius indenter yield strength. See Table 1 for a list of the indentation measurements.

observations in plastic flow strengths for He, W, and He + W irradiation. In addition, the merits of spherical nanoindentation stress–strain protocols for studying ion-irradiated materials will be discussed.

Appropriate hardening models for helium bubbles

Other experimental studies have typically reported small bubbles as weak to moderate obstacles using the FKH model or DBH model with a barrier strength of ~ 0.2 [68, 76, 77]. However, there are also reports [78–80] that have found that the hardening due to He bubbles is better described by the model proposed by Osetsky and Bacon [66]. One possible reason for the

range (weak versus strong barrier) reported in literature for He bubbles could be that describing the morphology with just the average values (e.g., diameter) is not sufficient. Sobie et al. [65] evaluated the DBH and BKS models using dislocation dynamics models for a variety of void morphologies and found that the BKS model provided accurate and consistent predictions using average values (e.g., diameter, spacing, etc.) while the DBH model could not. In other words, there was a linear relationship between predicted and simulated hardening for a range of void morphologies for the BKS model. Similarly, Sobie et al. [65] showed that the FKH model was also insensitive to differences in morphology that were not captured in the average values for self-interstitial atom loops. Therefore, the discrepancy in literature is not likely due to morphology differences when using the BKS model (and likely the OS model given their similarities) and FKH model. It also seems unlikely that morphological differences could explain significant differences (0.2 compared to 0.5 barrier strength) for the DBH model.

Another potential reason for the discrepancy in literature about hardening due to bubbles could be that the hardening is dependent on the He concentration to displacement damage ratio or something similar. One source of evidence to support this comes from simulations that have shown He-vacancy clusters, not observable with TEM, are likely to form and contribute significantly to the hardening [81–84], and the hardening from the clusters increases with an increasing ratio of helium atoms to vacancies [81]. Hardening due to He-vacancy clusters is supported by experimental observations of an increase in hardness despite no observations of bubbles [12]. Note in the case where bubbles are observed, it is unlikely that a large number of the He-vacancy clusters still exist since they are probable nucleation sites and/or absorbed by other bubbles. It is possible the hardening dependency on the He to vacancy ratio observed for clusters plays a role for small bubbles as well. Additionally, Trinkaus and Singh [85] have pointed out that there appears to be a critical He concentration below which hardening is less significant, and this critical point is dependent on different implantation factors (e.g., He concentration to dpa ratio, dose rate). Therefore, it seems likely that the discrepancy from the literature on the hardening due to He bubbles is due to the varying amounts of He concentration with respect to the displacement

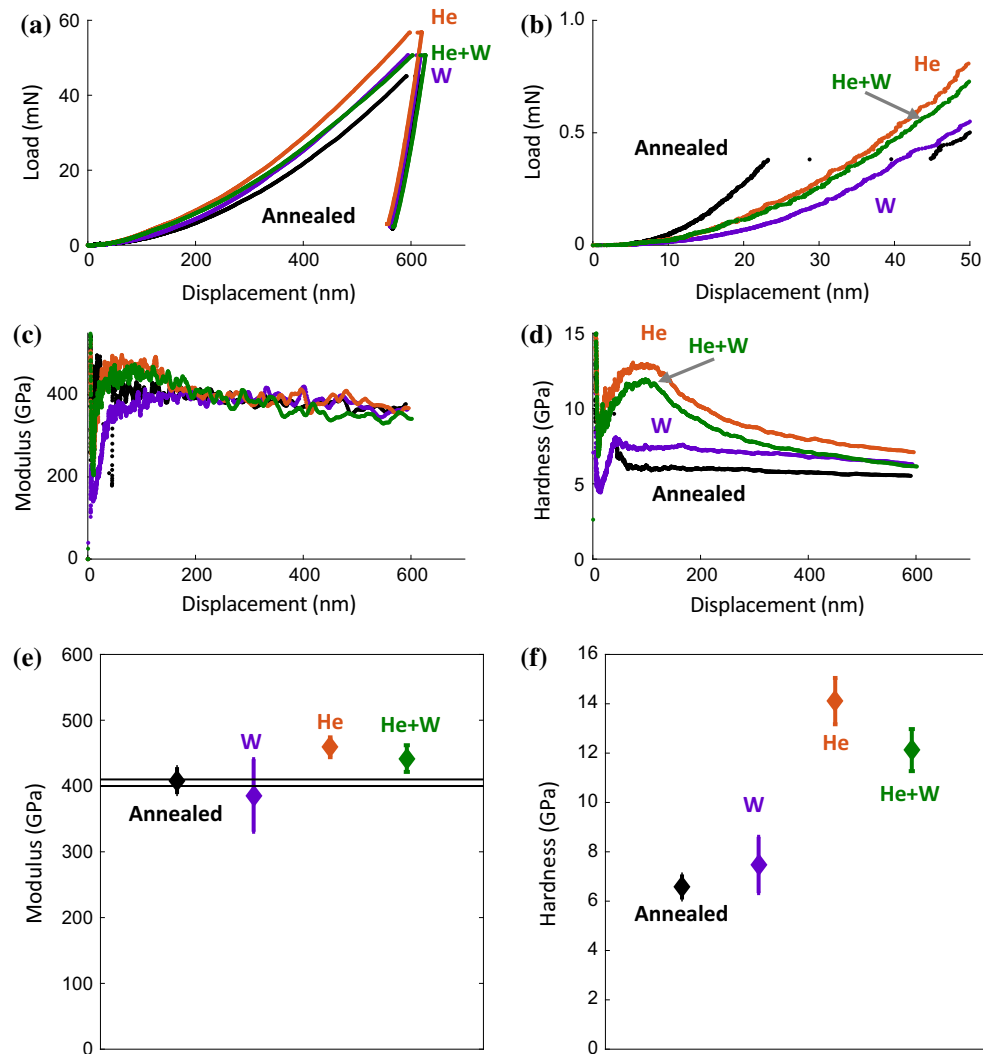


Figure 7 Berkovich nanoindentation **a** load–displacement curves, **b** load–displacement curves focused on the first 50 nm, **c** Young’s modulus versus displacement, **d** hardness versus displacement for annealed and irradiated conditions. Average **e** Young’s modulus and **f** hardness measurements from 12, 8, 9, and 9 tests on unirradiated (annealed) and irradiated (W, He, He + W), respectively. The average hardness was determined using the maximum

hardness between an indentation depth of 100 and 200 nm for each test. The average modulus was determined using the average modulus between an indentation depth of 100 and 200 nm for each test. Error bars are \pm one standard deviation. The solid lines on the modulus plot represent the expected Young’s modulus value between 400 and 410 GPa. See the supplemental material for a table of the average values.

damage. For example, the ratio of He concentration to displacement damage in this study is ~ 1.5 – 3.0 at.% / dpa, while for most studies it is $\ll 1$ at.% per dpa.

The models that provide the best predictions of the indentation yield strength of the constant implanted layer are based on modeling voids or Orowan hardening behavior (BKS and OS) or require an empirical factor representative of moderate to high barrier strength (DBH). Therefore, He bubbles in these experiments (high concentrations, small size, and

room temperature) represent moderate to strong barriers to dislocation slip. Models which predict when He bubbles will be weak or strong barriers are still required to unify the body of the literature on this subject. Selecting a single model for He bubbles from those explored is too complicated at present due to the uncertainty in the plastic flow strength of the constant irradiated layer and potentially missing physics from the models themselves based on discrepancies across literature.

Nanomechanical test protocols for studying ion-irradiated materials

Similar studies have also reported significant increases in the strength of He-implanted tungsten compared to W-irradiated tungsten using nanomechanical test protocols [11–13, 75, 86]. Hardie et al. [87] critically evaluated nanoindentation using the Oliver–Pharr method [41, 88] for different tip geometries (i.e., Berkovich, cube corner, and spherical) for making meaningful property measurements (e.g., hardness and modulus) from a small irradiated layer at the surface on Fe12%Cr. As a comparison between spherical and Berkovich nanoindentation, we also performed Berkovich nanoindentation using the Oliver–Pharr method [41] shown in Fig. 7. From Hardie et al. [87], we estimate the plastic zones under the Berkovich tip to be primarily within the constant irradiated layer up to a depth of 100 nm displacement. A more accurate estimate requires cross-sectional TEM under indents for each condition. The average hardness of the irradiated layer (Fig. 7f) was estimated as the maximum value between 100 and 200 nm displacement. There are three main similarities between the hardness and spherical indentation data: He-implanted conditions (He and He + W) have similar hardness values, both give higher peak hardness than W-irradiated condition, and at larger depths the hardness values start to converge to the unirradiated material. Trying to estimate the strength of the constant irradiated layer requires a deconvolution of the indentation size effect, He concentration gradient, plastic zone size evolution, work hardening, etc. It becomes apparent that the interpretation of the hardness versus displacement data is very complex. Other researchers have argued that indenting perpendicular to the damage gradient is best practice because the material probed has a constant amount of damage with indentation depth (no gradients in the indentation direction and no unirradiated material at larger depths) [89]. Reliable measurements certainly become less tedious (a well-polished sharp edge is still required); however, it is not very practical for He-implanted surfaces which typically go less than micron in depth.

Lastly, there is a long legacy of hardness (nano and micro) measurements for nuclear reactor materials with empirical correlations to uniaxial properties; however, there is potentially more information contained in the indentation stress–strain response as

presented in this work. The indentation stress–strain curve potentially provides a more rigorous experimental measurement compared to load–displacement or hardness–displacement curves for calibrating existing models in the literature (e.g., [90, 91]). One drawback of indentation measurements is that they do not directly give rise to estimates of changes in ductility to irradiation hardening. Thus, other nanomechanical tests such as micropillars, micro-tensile, and micro-cantilever beam bending are still required to understand changes in ductility in ion-irradiated layers.

Conclusions

This work employed novel spherical nanoindentation stress–strain protocols with careful characterization of the structure at the indentation site to reliably measure the mechanical effects of radiation damage from He implantation and W irradiation. There are multiple conclusions that can be drawn from this study:

1. Spherical nanoindentation stress–strain measurements showed higher plastic flow strengths for He-implanted tungsten (6.3–10.3 GPa) than W-irradiated tungsten (3.4 GPa) for the same displacement damage of 0.5 dpa at room temperature. Hardening calculations based on TEM measurements of the He bubbles and dislocation loops are in good agreement with this observation.
2. Spherical nanoindentation stress–strain measurements showed the same plastic flow strengths for He-implanted tungsten (6.3–10.3 GPa) as He + W-irradiated tungsten (5.7–10.3 GPa) despite the differences in displacement damage (0.5 dpa for He and 1.0 dpa for He + W). Hardening calculations based on TEM measurements of the He bubbles and dislocation loops are also in good agreement with this observation showing the contribution from dislocation loops (the additional 0.5 dpa in the He + W compared to just He) is not significant.
3. The defect structure of 1.0 dpa He + W irradiation in tungsten at room temperature resulted in a bubble density and diameter of $\sim 9.1 \times 10^{23} \text{ m}^{-3}$ and $\sim 1.1 \text{ nm}$ and dislocation loop density and diameter of $\sim 3 \times 10^{23} \text{ m}^{-3}$ and $\sim 3 \text{ nm}$,

respectively. In addition, the He bubble density and size remained unchanged going from He to He + W irradiation.

4. He bubbles acted as moderate to strong barriers ($\alpha = \sim 0.5\text{--}0.8$ for DBH model and agreement with void hardening model by OB) to dislocation slip, while dislocation loops acted as weak to moderate barriers ($\alpha = 0.1\text{--}0.3$ for DBH model). The large range in the barrier strength for He bubbles reflects the uncertainty in the plastic flow strength of the constant irradiated layer primarily due to the gradient in He concentration/damage. While the uncertainty in the barrier strength of the loops is primarily due to the uncertainty in indentation measurements on the annealed, unirradiated and irradiated material for a relatively small change in indentation strength.
5. The BKS, OS, and DBH models provide good predictions of the changes in the indentation yield strength due to dislocation loops and He bubbles. The FKH model provides a poor prediction for the change in yield strength due to the He bubbles.
6. Grain orientation effects on the indentations stress–strain response become less significant in the irradiated material compared to the annealed, unirradiated material.

Acknowledgements

The authors acknowledge funding from Department of Energy, Nuclear Engineering Enabling Technologies (DOE-NEET)—Reactor Materials program # DE-FOA-0000799, and University of California Office of the President (UCOP) Research Fund under Award Number 12-LR-237801 for this work. This work was performed, in part, at the Center for Integrated Nanotechnologies, an Office of Science User Facility operated for the US Department of Energy (DOE) Office of Science. Los Alamos National Laboratory, an affirmative action equal opportunity employer, is operated by Los Alamos National Security, LLC, for the National Nuclear Security Administration of the US Department of Energy under contract DE-AC52-06NA25396. SP gratefully acknowledges funding from the Los Alamos National Laboratory Director's Postdoctoral Fellowship and University of Nevada, Reno start-up faculty funds for this work.

Compliance with ethical standards

Conflicts of interest The authors have no conflicts of interest with regard to the research presented in this article.

Electronic supplementary material: The online version of this article (<https://doi.org/10.1007/s10853-017-1833-8>) contains supplementary material, which is available to authorized users.

References

- [1] Rieth M, Dudarev SL, de Vicente SMG, Aktaa J, Ahlgren T, Autusch S, Armstrong DEJ, Balden M, Baluc N, Barthe MF, Basuki WW, Battabyal M, Becquart CS, Blagoeva D, Boldyryeva H, Brinkmann J, Celino M, Ciupinski L, Correia JB, De Backer A, Domain C, Gaganidze E, Garcia-Rosales C, Gibson J, Gilbert MR, Giusepponi S, Gludovatz J, Greuner H, Heinola K, Hoschen T, Hoffmann A, Holstein N, Koch F, Krauss W, Li H, Lindig S, Linke J, Linsmeier C, Lopez-Ruiz P, Maier H, Matejicek J, Mishra TP, Muhammed M, Munoz A, Muzyk M, Nordlund K, Nguyen-Manh D, Opschoor J, Ordas N, Palacios T, Pintsuk G, Pippan R, Reiser J, Riesch J, Roberts SG, Romaner L, Rosinski M, Sanchez M, Schulmeyer W, Traxler H, Urena A, van der Laan JG, Veleva L, Wahlberg S, Walter M, Weber T, Weitkamp T, Wurster S, Yar MA, You JH, Zivelonghi A (2013) Recent progress in research on tungsten materials for nuclear fusion applications in Europe. *J Nucl Mater* 432(1–3):482–500. <https://doi.org/10.1016/j.jnucmat.2012.08.018>
- [2] Zinkle SJ, Busby JT (2009) Structural materials for fission & fusion Energy. *Mater Today* 12(11):12–19
- [3] Knaster J, Moeslang A, Muroga T (2016) Materials research for fusion. *Nat Phys* 12(5):424–434. <https://doi.org/10.1038/nphys3735>
- [4] Zinkle SJ, Was GS (2013) Materials challenges in nuclear energy. *Acta Mater* 61(3):735–758. <https://doi.org/10.1016/j.actamat.2012.11.004>
- [5] Zinkle SJ, Snead LL (2014) Designing radiation resistance in materials for fusion energy. In: Clarke DR (ed) *Annual Review of Materials Research*, vol 44. Annual Review of Materials Research. pp 241–267. <https://doi.org/10.1146/annurev-matsci-070813-113627>
- [6] Was GS (2007) *Fundamentals of radiation materials science*. Springer, New York
- [7] Was GS, Busby JT, Allen T, Kenik EA, Jenssen A, Bruemmer SM, Gan J, Edwards AD, Scott PM (2002)

- Emulation of neutron irradiation effects with protons: validation of principle. *J Nucl Mater* 300(2–3):198–216. [https://doi.org/10.1016/s0022-3115\(01\)00751-6](https://doi.org/10.1016/s0022-3115(01)00751-6)
- [8] Hosemann P, Swadener JG, Kiener D, Was GS, Maloy SA, Li N (2008) An exploratory study to determine applicability of nano-hardness and micro-compression measurements for yield stress estimation. *J Nucl Mater* 375(1):135–143. <https://doi.org/10.1016/j.jnucmat.2007.11.004>
- [9] Kiener D, Hosemann P, Maloy SA, Minor AM (2011) In situ nanocompression testing of irradiated copper. *Nat Mater* 10(8):608–613. <https://doi.org/10.1038/nmat3055>
- [10] Li N, Mara NA, Wang YQ, Nastasi M, Misra A (2011) Compressive flow behavior of Cu thin films and Cu/Nb multilayers containing nanometer-scale helium bubbles. *Scr Mater* 64(10):974–977. <https://doi.org/10.1016/j.scriptamat.2011.02.001>
- [11] Armstrong DEJ, Yi X, Marquis EA, Roberts SG (2013) Hardening of self ion implanted tungsten and tungsten 5-wt% rhenium. *J Nucl Mater* 432(1–3):428–436. <https://doi.org/10.1016/j.jnucmat.2012.07.044>
- [12] Armstrong DEJ, Edmondson PD, Roberts SG (2013) Effects of sequential tungsten and helium ion implantation on nano-indentation hardness of tungsten. *Appl Phys Lett*. <https://doi.org/10.1063/1.4811825>
- [13] Armstrong DEJ, Hardie CD, Gibson J, Bushby AJ, Edmondson PD, Roberts SG (2015) Small-scale characterization of irradiated nuclear materials: part II nanoindentation and micro-cantilever testing of ion irradiated nuclear materials. *J Nucl Mater* 462:374–381. <https://doi.org/10.1016/j.jnucmat.2015.01.053>
- [14] James G, David A (2014) Steve R (2014) The micro-mechanical properties of ion irradiated tungsten. *Phys Scr* T159:014056
- [15] Weaver JS, Pathak S, Reichardt A, Vo HT, Maloy SA, Hosemann P, Mara NA (2017) Spherical nanoindentation of proton irradiated 304 stainless steel: a comparison of small scale mechanical test techniques for measuring irradiation hardening. *J Nucl Mater* 493:368–379
- [16] Herbert EG, Pharr GM, Oliver WC, Lucas BN, Hay JL (2001) On the measurement of stress-strain curves by spherical indentation. *Thin Solid Films* 398:331–335. [https://doi.org/10.1016/s0040-6090\(01\)01439-0](https://doi.org/10.1016/s0040-6090(01)01439-0)
- [17] Basu S, Moseson A, Barsoum MW (2006) On the determination of spherical nanoindentation stress-strain curves. *J Mater Res* 21(10):2628–2637. <https://doi.org/10.1557/jmr.2006.0324>
- [18] Kalidindi SR, Pathak S (2008) Determination of the effective zero-point and the extraction of spherical nanoindentation stress-strain curves. *Acta Mater* 56(14):3523–3532. <https://doi.org/10.1016/j.actamat.2008.03.036>
- [19] Field JS, Swain MV (1995) Determining the mechanical properties of small volumes of material from submicrometer spherical indentations. *J Mater Res* 10(1):101–112. <https://doi.org/10.1557/jmr.1995.0101>
- [20] Field JS, Swain MV (1993) A simple predictive model for spherical indentation. *J Mater Res* 8(2):297–306. <https://doi.org/10.1557/jmr.1993.0297>
- [21] Hertz H, Jones DE, Schott GA (1896) *Miscellaneous papers*. Macmillan and co, London, New York
- [22] Johnson KL (1985) *Contact mechanics*. Cambridge University Press, Cambridge, New York
- [23] Tabor D (1951) The hardness and strength of metals. *J Inst Met* 79(1):1–18
- [24] Pathak S, Kalidindi SR (2015) Spherical nanoindentation stress-strain curves. *Mat Sci Eng R* 91:1–36. <https://doi.org/10.1016/j.mser.2015.02.001>
- [25] Pathak S, Shaffer J, Kalidindi SR (2009) Determination of an effective zero-point and extraction of indentation stress-strain curves without the continuous stiffness measurement signal. *Scr Mater* 60(6):439–442. <https://doi.org/10.1016/j.scriptamat.2008.11.028>
- [26] Pathak S, Kalidindi SR, Weaver JS, Wang Y, Doerner R, Mara NA (accepted) Probing nanoscale damage gradients in ion-irradiated metals using spherical nanoindentation. *Scientific Reports*
- [27] Pathak S, Kalidindi SR, Mara NA (2016) Investigations of orientation and length scale effects on micromechanical responses in polycrystalline zirconium using spherical nanoindentation. *Scr Mater* 113:241–245. <https://doi.org/10.1016/j.scriptamat.2015.10.035>
- [28] Pathak S, Stojakovic D, Kalidindi SR (2009) Measurement of the local mechanical properties in polycrystalline samples using spherical nanoindentation and orientation imaging microscopy. *Acta Mater* 57(10):3020–3028. <https://doi.org/10.1016/j.actamat.2009.03.008>
- [29] Weaver JS, Priddy MW, McDowell DL, Kalidindi SR (2016) On capturing the grain-scale elastic and plastic anisotropy of alpha-Ti with spherical nanoindentation and electron back-scattered diffraction. *Acta Mater* 117:23–34. <https://doi.org/10.1016/j.actamat.2016.06.053>
- [30] Weaver JS, Khosravani A, Castillo A, Kalidindi SR (2016) High throughput exploration of process-property linkages in Al-6061 using instrumented spherical microindentation and microstructurally graded samples. *Integr Mater Manuf Innov* 5(1):1–20. <https://doi.org/10.1186/s40192-016-0054-3>
- [31] Weaver JS, Kalidindi SR (2016) Mechanical characterization of Ti-6Al-4 V titanium alloy at multiple length scales using spherical indentation stress-strain measurements. *Mater Des* 111:463–472. <https://doi.org/10.1016/j.matdes.2016.09.016>

- [32] Vachhani SJ, Kalidindi SR (2015) Grain-scale measurement of slip resistances in aluminum polycrystals using spherical nanoindentation. *Acta Mater* 90:27–36. <https://doi.org/10.1016/j.actamat.2015.02.017>
- [33] Patel DK, Kalidindi SR (2016) Correlation of spherical nanoindentation stress-strain curves to simple compression stress-strain curves for elastic-plastic isotropic materials using finite element models. *Acta Mater* 112:295–302. <https://doi.org/10.1016/j.actamat.2016.04.034>
- [34] Patel DK, Al-Harbi HF, Kalidindi SR (2014) Extracting single-crystal elastic constants from polycrystalline samples using spherical nanoindentation and orientation measurements. *Acta Mater* 79:108–116. <https://doi.org/10.1016/j.actamat.2014.07.021>
- [35] Donohue BR, Ambrus A, Kalidindi SR (2012) Critical evaluation of the indentation data analyses methods for the extraction of isotropic uniaxial mechanical properties using finite element models. *Acta Mater* 60(9):3943–3952. <https://doi.org/10.1016/j.actamat.2012.03.034>
- [36] Patel DK, Kalidindi SR Estimating the slip resistance from spherical nanoindentation and orientation measurements in polycrystalline samples of cubic metals. *Int J Plasticity*. <http://dx.doi.org/10.1016/j.ijplas.2017.03.004>
- [37] Ziegler JF, Biersack JP (2008) SRIM Program. IBM Corp, Yorktown
- [38] Pathak S, Riesterer JL, Kalidindi SR, Michler J (2014) Understanding pop-ins in spherical nanoindentation. *Appl Phys Lett* 105(16):161913. <https://doi.org/10.1063/1.4898698>
- [39] Phani PS, Johanns KE, George EP, Pharr GM (2013) A stochastic model for the size dependence of spherical indentation pop-in. *J Mater Res* 28(19):2728–2739. <https://doi.org/10.1557/Jmr.2013.254>
- [40] Shim S, Bei H, George EP, Pharr GM (2008) A different type of indentation size effect. *Scr Mater* 59(10):1095–1098. <https://doi.org/10.1016/j.scriptamat.2008.07.026>
- [41] Oliver WC, Pharr GM (2004) Measurement of hardness and elastic modulus by instrumented indentation: advances in understanding and refinements to methodology. *J Mater Res* 19(1):3–20. <https://doi.org/10.1557/jmr.2004.19.1.3>
- [42] Jenkins ML, Kirk MA (2000) Characterisation of radiation damage by transmission electron microscopy. CRC Press, Boca Raton
- [43] Pathak S (2012) Studying grain boundary regions in polycrystalline materials using spherical nano-indentation and orientation imaging microscopy. *J Mater Sci*. <https://doi.org/10.1007/s10853-011-5859-z>
- [44] Kalidindi SR, Vachhani SJ (2014) Mechanical characterization of grain boundaries using nanoindentation. *Curr Opin Solid State Mat Sci* 18(4):196–204. <https://doi.org/10.1016/j.cossms.2014.05.002>
- [45] Vachhani SJ, Trujillo C, Mara N, Livescu V, Bronkhorst C, Gray GT, Cerreta E (2016) Local mechanical property evolution during high strain-rate deformation of tantalum. *J Dyn Behav Mater* 2(4):511–520
- [46] Tabor D (1951) *The hardness of metals*. Clarendon Press, Oxford
- [47] Tabor D (1956) The physical meaning of indentation and scratch hardness. *Br J Appl Phys* 7(5):159
- [48] Zhang P, Li SX, Zhang ZF (2011) General relationship between strength and hardness. *Mater Sci Eng, A*. <https://doi.org/10.1016/j.msea.2011.08.061>
- [49] Patel DK, Kalidindi SR (2017) Estimating the slip resistance from spherical nanoindentation and orientation measurements in polycrystalline samples of cubic metals. *Int J Plast* 92:19–30
- [50] Nix WD, Gao HJ (1998) Indentation size effects in crystalline materials: a law for strain gradient plasticity. *J Mech Phys Solids* 46(3):411–425. [https://doi.org/10.1016/S0022-5096\(97\)00086-0](https://doi.org/10.1016/S0022-5096(97)00086-0)
- [51] Pharr GM, Herbert EG, Gao YF (2010) The indentation size effect: a critical examination of experimental observations and mechanistic interpretations. *Annu Rev Mater Res* 40:271–292. <https://doi.org/10.1146/annurev-matsci-070909-104456>
- [52] Durst K, Göken M, Pharr GM (2008) Indentation size effect in spherical and pyramidal indentations. *J Phys D Appl Phys* 41(7):074005
- [53] Michalske T, Houston J (1998) Dislocation nucleation at nano-scale mechanical contacts. *Acta Mater* 46(2):391–396
- [54] Suresh S, Nieh T-G, Choi B (1999) Nano-indentation of copper thin films on silicon substrates. *Scr Mater* 41(9):951–957
- [55] Swadener JG, George EP, Pharr GM (2002) The correlation of the indentation size effect measured with indenters of various shapes. *J Mech Phys Solids* 50(4):681–694. [https://doi.org/10.1016/S0022-5096\(01\)00103-X](https://doi.org/10.1016/S0022-5096(01)00103-X)
- [56] Huang Y, Zhang F, Hwang KC, Nix WD, Pharr GM, Feng G (2006) A model of size effects in nano-indentation. *J Mech Phys Solids* 54(8):1668–1686. <https://doi.org/10.1016/j.jmps.2006.02.002>
- [57] Pathak S, Michler J, Wasmer K, Kalidindi SR (2012) Studying grain boundary regions in polycrystalline materials using spherical nano-indentation and orientation imaging microscopy. *J Mater Sci* 47(2):815–823. <https://doi.org/10.1007/s10853-011-5859-z>
- [58] Bushby AJ, Roberts SG, Hardie CD (2012) Nanoindentation investigation of ion-irradiated Fe–Cr alloys using spherical indenters. *J Mater Res* 27(1):85–90

- [59] Ahn T-H, Lee SB, Park K-T, Oh KH, Han HN (2014) Strain-induced ϵ -martensite transformation during nanoindentation of high-nitrogen steel. *Mater Sci Eng, A* 598:56–61. <https://doi.org/10.1016/j.msea.2014.01.030>
- [60] Misra RDK, Zhang Z, Jia Z, Surya PKCV, Somani MC, Karjalainen LP (2011) Nanomechanical insights into the deformation behavior of austenitic alloys with different stacking fault energies and austenitic stability. *Mater Sci Eng, A* 528(22–23):6958–6963. <https://doi.org/10.1016/j.msea.2011.05.068>
- [61] Nembach E (1996) Particle strengthening of metals and alloys. Wiley, New York
- [62] Kroupa F, Hirsch PB (1964) Elastic interaction between prismatic dislocation loops and straight dislocations. *Discuss Faraday Soc* 38:49–55. <https://doi.org/10.1039/df9643800049>
- [63] Friedel J (1963) On the elastic limit of crystals. In: Thomas G, Washburn J (eds) *Electron Microscopy and Strength of Crystals*. Interscience, New York, p 605
- [64] Bacon DJ, Kocks UF, Scattergood RO (1973) Effect of dislocation self-interaction on Orowan stress. *Philos Mag* 28(6):1241–1263. <https://doi.org/10.1080/14786437308227997>
- [65] Sobie C, Bertin N, Capolungo L (2015) Analysis of obstacle hardening models using dislocation dynamics: application to irradiation-induced defects. *Metall Mater Trans Phys Metall Mater Sci* 46A(8):3761–3772. <https://doi.org/10.1007/s11661-015-2935-z>
- [66] Osetsky YN, Bacon DJ (2010) Atomic-scale mechanisms of void hardening in bcc and fcc metals. *Philos Mag* 90(7–8):945–961. <https://doi.org/10.1080/14786430903164580>
- [67] Hirth JP, Lothe J (1982) *Theory of Dislocations*. Wiley, New York
- [68] Odette GR, Frey D (1979) Development of mechanical property correlation methodology for fusion environments. *J Nucl Mater* 85-6 (DEC):817-822. [https://doi.org/10.1016/0022-3115\(79\)90360-x](https://doi.org/10.1016/0022-3115(79)90360-x)
- [69] Queyreau S, Monnet G, Devincre B (2010) Orowan strengthening and forest hardening superposition examined by dislocation dynamics simulations. *Acta Mater* 58(17):5586–5595. <https://doi.org/10.1016/j.actamat.2010.06.028>
- [70] Zhang Z, Hasenhuettl E, Yabuuchi K, Kimura A (2016) Evaluation of helium effect on ion-irradiation hardening in pure tungsten by nano-indentation method. *Nucl Mater Energy* 9:539–546
- [71] Morris JR, Bei H, Pharr GM, George EP (2011) Size effects and stochastic behavior of nanoindentation pop in. *Phys Rev Lett*. <https://doi.org/10.1103/PhysRevLett.106.165502>
- [72] Wang Z, Bei H, George EP, Pharr GM (2011) Influences of surface preparation on nanoindentation pop-in in single-crystal Mo. *Scr Mater* 65(6):469–472. <https://doi.org/10.1016/j.scriptamat.2011.05.030>
- [73] Armstrong D, Wilkinson A, Roberts S (2011) Mechanical properties of ion-implanted tungsten–5 wt% tantalum. *Phys Scr T145*:014076
- [74] Miyamoto M, Nishijima D, Baldwin M, Doerner R, Ueda Y, Yasunaga K, Yoshida N, Ono K (2011) Microscopic damage of tungsten exposed to deuterium–helium mixture plasma in PISCES and its impacts on retention property. *J Nucl Mater* 415(1):S657–S660
- [75] Hu X, Koyanagi T, Fukuda M, Kumar NAPK, Snead LL, Wirth BD, Katoh Y (2016) Irradiation hardening of pure tungsten exposed to neutron irradiation. *J Nucl Mater* 480:235–243. <https://doi.org/10.1016/j.jnucmat.2016.08.024>
- [76] Lucas GE (1993) The evolution of mechanical property change in irradiated austenitic stainless steels. *J Nucl Mater* 206(2):287–305. [https://doi.org/10.1016/0022-3115\(93\)90129-M](https://doi.org/10.1016/0022-3115(93)90129-M)
- [77] Sun C, Yu KY, Lee JH, Liu Y, Wang H, Shao L, Maloy SA, Hartwig KT, Zhang X (2012) Enhanced radiation tolerance of ultrafine grained Fe–Cr–Ni alloy. *J Nucl Mater* 420(1–3):235–240. <https://doi.org/10.1016/j.jnucmat.2011.10.001>
- [78] Li N, Nastasi M, Misra A (2012) Defect structures and hardening mechanisms in high dose helium ion implanted Cu and Cu/Nb multilayer thin films. *Int J Plast* 32–33:1–16. <https://doi.org/10.1016/j.ijplas.2011.12.007>
- [79] Wei QM, Li N, Mara N, Nastasi M, Misra A (2011) Suppression of irradiation hardening in nanoscale V/Ag multilayers. *Acta Mater* 59(16):6331–6340. <https://doi.org/10.1016/j.actamat.2011.06.043>
- [80] Yu KY, Liu Y, Fu EG, Wang YQ, Myers MT, Wang H, Shao L, Zhang X (2013) Comparisons of radiation damage in He ion and proton irradiated immiscible Ag/Ni nanolayers. *J Nucl Mater* 440(1–3):310–318. <https://doi.org/10.1016/j.jnucmat.2013.04.069>
- [81] Yang L, Zu XT, Gao F, Peng SM, Heinisch HL, Long XG, Kurtz RJ (2010) Dynamic interactions of helium-vacancy clusters with edge dislocations in α -Fe. *Phys B: Condens Matter* 405(7):1754–1758. <https://doi.org/10.1016/j.physb.2010.01.034>
- [82] Hafez Haghghat SM, Schaeublin R (2008) Molecular dynamics modeling of cavity strengthening in irradiated iron. *J Comput Aided Mater Des* 14(1):191. <https://doi.org/10.1007/s10820-007-9065-x>
- [83] Schäublin R, Chiu YL (2007) Effect of helium on irradiation-induced hardening of iron: a simulation point of view. *J Nucl Mater* 362(2–3):152–160. <https://doi.org/10.1016/j.jnucmat.2007.01.187>
- [84] Wang YX, Xu Q, Yoshiie T, Pan ZY (2008) Effects of edge dislocations on interstitial helium and helium cluster

- behavior in alpha-Fe. *J Nucl Mater* 376(2):133–138. <https://doi.org/10.1016/j.jnucmat.2008.02.066>
- [85] Trinkaus H, Singh BN (2003) Helium accumulation in metals during irradiation – where do we stand? *J Nucl Mater* 323(2–3):229–242. <https://doi.org/10.1016/j.jnucmat.2003.09.001>
- [86] Gibson JSKL, Roberts SG, Armstrong DEJ (2015) High temperature indentation of helium-implanted tungsten. *Mater Sci Eng, A* 625:380–384. <https://doi.org/10.1016/j.msea.2014.12.034>
- [87] Hardie CD, Roberts SG, Bushby AJ (2015) Understanding the effects of ion irradiation using nanoindentation techniques. *J Nucl Mater* 462:391–401. <https://doi.org/10.1016/j.jnucmat.2014.11.066>
- [88] Oliver WC, Pharr GM (1992) An improved technique for determining hardness and elastic-modulus using load and displacement sensing indentation experiments. *J Mater Res* 7(6):1564–1583. <https://doi.org/10.1557/jmr.1992.1564>
- [89] Hosemann P, Kiener D, Wang YQ, Maloy SA (2012) Issues to consider using nano indentation on shallow ion beam irradiated materials. *J Nucl Mater* 425(1–3):136–139. <https://doi.org/10.1016/j.jnucmat.2011.11.070>
- [90] Patra A, McDowell DL (2016) Crystal plasticity investigation of the microstructural factors influencing dislocation channeling in a model irradiated bcc material. *Acta Mater* 110:364–376. <https://doi.org/10.1016/j.actamat.2016.03.041>
- [91] Dunn A, Dingreville R, Capolungo L (2016) Multi-scale simulation of radiation damage accumulation and subsequent hardening in neutron-irradiated α -Fe. *Model Simul Mater Sci Eng* 24(1):015005